Shock Waves (2001) 10: 405–420

Shock Waves

Nonideal effects behind reflected shock waves in a high-pressure shock tube*

Eric L. Petersen[1], Ronald K. Hanson[2]

[1] The Aerospace Corporation, Propulsion Science & Experimental Mechanics, El Segundo, CA 90245, USA
[2] Stanford University, Thermosciences Division, Department of Mechanical Engineering, Stanford, CA 94305, USA

Received 25 April 2000 / Accepted 8 September 2000

Abstract. Shock tubes often experience temperature and pressure nonuniformities behind the reflected shock wave that cannot be neglected in chemical kinetics experiments. Because of increased viscous effects, smaller tube diameters, and nonideal shock formation, the reflected-shock nonidealities tend to be greater in higher-pressure shock tubes. Since the increase in test temperature (ΔT_5) is the most significant parameter for chemical kinetics, experiments were performed to characterize ΔT_5 in the Stanford High Pressure Shock Tube using infrared emission from a known amount of CO in argon. From the measured change in vibrationally equilibrated CO emission with time, the corresponding $\mathrm{d}T_5/\mathrm{d}t$ (or ΔT_5 for a known time interval) of the mixture was inferred assuming an isentropic relationship between post-shock temperature and pressure changes. For a range of representative conditions in argon (24–530 atm, 1275–1900 K), the test temperature 2 cm from the endwall increased 3–8 K after 100 µs and 15–40 K after 500 µs, depending on the initial conditions. Separate pressure measurements using a shielded piezoelectric transducer confirmed the isentropic assumption. An analytical model of the reflected-shock gas dynamics was also developed, and the calculated ΔT_5's agree well with those obtained from experiment. The analytical model was used to estimate the effects of temperature and pressure nonuniformities on typical chemical kinetics measurements. When the kinetics are fast (< 300 µs), the temperature increase is typically negligible, although some correction is suggested for kinetics experiments lasting longer than 500 µs. The temperature increase, however, has a negligible impact on the measured laser absorption profiles of OH (306 nm) and CH_3 (216 nm), validating the use of a constant absorption coefficient. Infrared emission experiments are more sensitive to temperature and density changes, so T_5 nonuniformities should be taken into account when interpreting ir-emission data.

Key words: Shock tube, Chemical kinetics, High pressure, Boundary layer, Laser absorption, ir emission

1 Introduction

Ideally, the temperature and pressure in the region behind reflected shock waves do not vary with time and are equal to the values calculated using classical theory. However, nonideal fluid mechanics such as incident-shock attenuation and boundary layer growth lead to temperatures and pressures behind the reflected shock wave that increase with time. Unfortunately, when performing chemistry measurements in a shock tube, errors in the reaction temperature can lead to large uncertainties in the rate coefficient or ignition delay time (Bowman and Hanson, 1979). For example, the high-pressure rate coefficient for the dissociation of NO_2 has an activation energy of 300 kJ/mol (i.e., $k_\infty(T) = 4 \times 10^{14} \exp(300/RT)$) (Röhrig et al., 1997). For an average temperature of 1500 K, a 15-K error in temperature (i.e., only 1%) can lead to a 25% error in the measured rate coefficient. Therefore, great care must be taken to minimize uncertainties in the shock-tube test temperature, and many experimental and analytical studies were conducted by previous investigators to characterize shock tube temperature nonuniformities and determine their impact on measurement accuracy.

Most temperature and density corrections for incident-shock chemistry measurements have been based on the area-reduction equations of Mirels (1963; 1964), which are simplified forms of the more-extensive boundary-layer routines developed in earlier papers by Mirels. Some examples of incident-shock nonuniformity studies include those of Warshay (1968), Belford and Strehlow (1969), Belles and Brabbs (1971; 1972), Bertin et al. (1975), Fujii et al. (1979), and Koshi and Asaba (1979). In general, boundary-layer effects behind the incident shock wave are more important for longer test times, and incident-shock measurements are further complicated by the particle-

---

Correspondence to: E.L. Petersen
(e-mail: Eric.L.Petersen@aero.org)

* When much of this work was performed, both authors were with Stanford University.

time correction. Performing measurements behind the reflected shock wave where the flow is (ideally) stagnant eliminates many of the time-dependent problems with incident-shock measurements.

Early reflected-shock studies, however, uncovered large errors in T_5 which could seriously impact reflected-shock chemistry measurements (Strehlow and Cohen, 1958; Skinner, 1959; Brabbs et al., 1960; Strehlow and Case, 1961). Strehlow and Cohen (1958) and Skinner (1959) attributed the uncertainties to shock-wave/boundary-layer interaction in other than monatomic gases. Underpredictions between 30 and 200 K were estimated, and Brabbs et al. (1960) observed significant reflected-shock temperature uncertainties even in argon. Strehlow and Case (1961) in a later study found that temperatures in argon were overpredicted instead of underpredicted, while Johnson and Britton (1963) claimed their Br decomposition measurements behind reflected shocks in an argon bath disagreed with similar data taken behind incident shock waves. Nitrous oxide decomposition measurements by Fishburne et al. (1964) likewise displayed a discrepancy between rates obtained behind reflected waves versus those measured behind incident waves.

Fortunately, later studies implicated errors in incident-shock velocity measurement, vibrational relaxation, test section location, etc. for the larger, unknown errors in reflected-shock temperature (Bowman and Hanson, 1979). Optical measurements of the temperature support the values of T_5 calculated from ideal theory, assuming the shock tube diameter is large enough to minimize attenuation affects, and the bifurcation structure in di- and polyatomic test gases is minor (Bowman and Hanson, 1979; Presley and Hanson, 1969).

Although the initial endwall T_5 is now routinely inferred from the incident-shock velocity, property variations behind the reflected shock wave due to incident-shock velocity attenuation and nonuniform incident-flow-field effects persist and must still be accounted for in certain cases. The test temperature and pressure vary because the reflected shock wave propagates into a gas that was processed by an attenuating incident shock wave with a boundary layer behind it. The perturbations in the nonuniform flow field upstream of the reflected shock lead to disturbance waves behind the reflected shock which influence the thermodynamic properties therein.

The present paper is concerned with nonideal conditions behind reflected shock waves in the Stanford High Pressure Shock Tube (HPST). Specifically, the temperature and pressure increase behind reflected shock waves in the HPST is characterized, and an analytical model that predicts the temperature rise behind the reflected shock wave for a given incident-shock velocity profile is presented. Finally, the effect of nonuniform temperature on typical reflected-shock chemical kinetics measurements in the HPST is presented in the form of high-pressure species-profile calculations and measurements.

2 Shock tube and attenuation

The Stanford HPST, described in detail by Petersen (1998), has a 3-m, 7.62-cm-dia driver and a 5-m, 5-cm-dia driven section. For most experiments, the driver gas is helium, and the test gas is predominantly argon. The shock tube uses steel or aluminum diaphragms in either a single- or double-diaphragm mode of operation. As mentioned above, a common indication of shock-tube ideality is the attenuation of the incident shock wave. On the HPST, the incident-shock velocity as a function of axial distance is measured via six fast-response piezoelectric pressure transducers (PCB 113A) and five Phillips PM6666 time-interval counters over roughly the last meter before the endwall. Typical shock attenuations, defined as the normalized slope of axial velocity as extrapolated to the endwall (in %/meter), range from 1 to 4%/m. The incident-shock attenuation in the HPST is due primarily to boundary layer layer buildup (Mirels, 1963; Mirels, 1964; Petersen, 1998) and nonideal rupture of the diaphragm(s) (Petersen, 1998).

Ideally, diaphragm breakage and shock formation occur instantaneously, but measurements by previous investigators indicate the diaphragm opening process can take hundreds of microseconds (Rothkopf and Low, 1974). The finite opening time of the diaphragm can affect the shock formation distance and trajectory (White, 1958; Simpson et al., 1967; Tajima et al., 1968; Ikui and Matsuo, 1969; Ikui et al., 1969; Outa et al., 1975; Rothkopf and Low, 1976) and, in general, slow-opening diaphragms cause the peak in axial shock trajectory to occur further downstream (Simpson et al., 1967). The resulting slope of the attenuating shock downstream of the peak Mach number can be steeper than predicted assuming viscous effects alone (Tajima et al., 1968). Opening time/formation distance has been found to vary inversely with driver-to-driven pressure difference, P_{41} (i.e, $P_4 - P_1$), and directly with diaphragm density, diaphragm thickness, ultimate stress of the diaphragm material, and shock tube diameter (Ikui and Matsuo, 1969). For the HPST, the shock-formation distance and diaphragm opening time are not routinely measured, but these cited trends qualitatively support the observed test-to-test variation in the incident-shock attenuation. Variations in the scribe depth (i.e., diaphragm thickness), total diaphragm material volume, and rate of P_4-filling (i.e, rate of stress on the diaphragm) for single-diaphragm experiments were found to contribute to deviations in the measured shock trajectory.

A representative range of attenuation data are presented as a function of incident-shock Mach number at the endwall (M_s) and fill pressure (P_1) in Fig. 1. If the attenuation were due solely to the viscous boundary layer, the attenuation would vary with Mach number and fill pressure per the calculated curve in Fig. 1 labeled as “model”. The model curve was derived using the analytical shock tube boundary layer models presented by Petersen (1998) and Mirels (1963; 1964). However, the actual attenuation data are higher than the calculated values and exhibit large scatter (±0.5%/m). The large scatter and higher attenuation indicate nonideal effects other than viscosity, such as

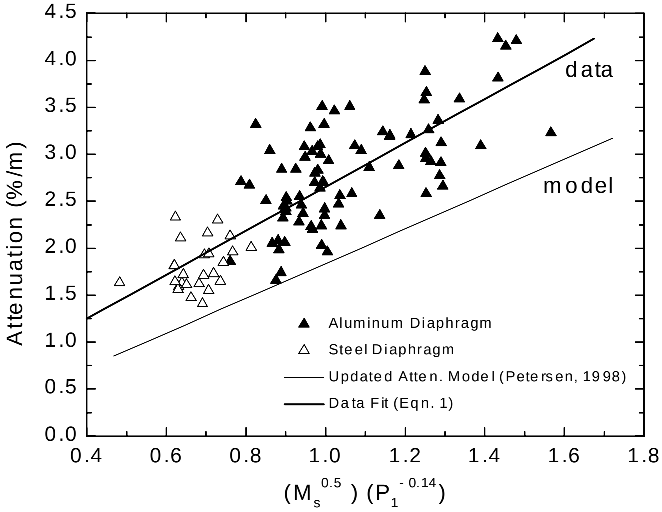

Fig. 1. Sample HPST incident-shock attenuation data in argon as a function of Mach number and fill pressure (in atm). The data are compared to the analytical shock-attenuation model of Petersen (1998) and Mirels (1963; 1964), which includes only viscous effects

nonideal diaphragm breakage and test-to-test variations in diaphragm thickness, contribute to the overall attenuation.

From the results of Fig. 1, one can conclude that wall viscous effects comprise approximately 70% (or more) of the total shock attenuation, while nonideal shock formation contributes the remaining 30% (or less). Nonetheless, the total attenuation varies roughly with M_s and P_1 as predicted by attenuation theory, i.e., $P_1^{-0.14}$ and $M_s^{0.5}$. The attenuation data can be fit to a correlation based on these parameters with r^2 of 0.64 as follows

$$\text{Attenuation (\%/m)} = 0.32 + 2.34 P_1^{-0.14} \sqrt{M_s}\,. \tag{1}$$

The line representing Eq. (1) is displayed in Fig. 1. This correlation can be used to estimate the attenuation in the HPST in lieu of direct measurements and/or for predictive calculations, but one should exercise caution due to the observed scatter in measured attenuation (Fig. 1). The steel diaphragms tend to produce lower attenuation than the aluminum diaphragms primarily because of the higher fill pressures involved, per Eq. (1) (note that higher fill pressures correspond to higher test, or P_5, pressures).

Perhaps the most significant aspect of the Fig. 1 attenuation data is the relatively high degree of incident-shock attenuation when compared to the ≈ 1%/m attenuation typically observed in many low-pressure shock tubes. A significant contributor to the increased attenuation is the enhanced effect of viscosity due in part to the higher pressure and the smaller tube diameter. Since the test pressure is often 2 to 3 orders of magnitude higher than in lower pressure shock tubes, the Reynolds number is higher, leading to a situation where the boundary layer can be assumed turbulent immediately behind the incident shock wave. The turbulent boundary layer results in a much thicker boundary layer than would exist if the layer were laminar at the same pressure (Petersen, 1998). The effects of test pressure and diameter on the turbulent boundary layer and the resulting reflected-shock nonuniformity are detailed in the analytical-model calculations below.

3 Temperature measurements

Although many experimenters use analytical methods to predict and correct for nonideal effects due to boundary layer growth and shock attenuation, actual measurements of the temperature and pressure changes are preferred. Therefore, measurements of the temperature increase behind reflected shock waves were performed in the HPST over a range of elevated pressures and are summarized in this section.

3.1 Background

Others have utilized various optical methods to explore and characterize the shocked-gas temperature in low-pressure shock tubes. For example, line reversal techniques have been employed to measure very high temperatures (Gaydon and Hurle, 1963; Parkinson and Nicholls, 1960; Napier et al., 1964; Tsuchiya and Kuratani, 1965). More recently, a rapid-tuning ring-dye laser was used to measure the temperature behind incident (Rea et al., 1984) and reflected (Chang et al., 1987) shock waves by taking the ratio of the $R_1(7)$ and $R_1(11)$ OH lines of the $A \leftarrow X$ transition near 306.5 nm; the OH was generated in an argon bath seeded with a stoichiometric $H_2{-}O_2$ mixture. The quoted accuracy for the laser-based absorption technique was 3%, or 40–100 K for the temperature ranges considered.

An alternate method for obtaining the hot-gas temperature in a shock tube involves monitoring the infrared emission from vibrationally excited molecules, present in small quantities. Once this minor constituent is vibrationally equilibrated, its temperature approaches the bulk-gas temperature and, through calibration of the optical setup, the bulk-gas temperature can be determined. Lapworth et al. (1971) and Guinee et al. (1980) used the carbon monoxide and carbon dioxide vibrational bands near 4.7 µm to measure the absolute reflected-shock temperature with a three-percent error.

A simpler method involves the measurement of ΔT only, so tedious calibration of the ir measurement apparatus is not needed (which, regardless, may not be accurate enough to discern temperature changes within 50 K). Just and Schmalz (CO) (1968), Flower (CO) (1976), Hayashi and Goto (CO_2) (1990), and Ciezki and Adomeit (CO_2) (1990) have used this ΔT method to characterize the temperature uniformity of post-shock gases in their respective facilities. In the present application, knowledge of the absolute temperature was not as important as measurement of the temperature increase, so an infrared emission technique was used to determine the temperature increase behind reflected shocks in the HPST. Details of the measurements and their results are described below.

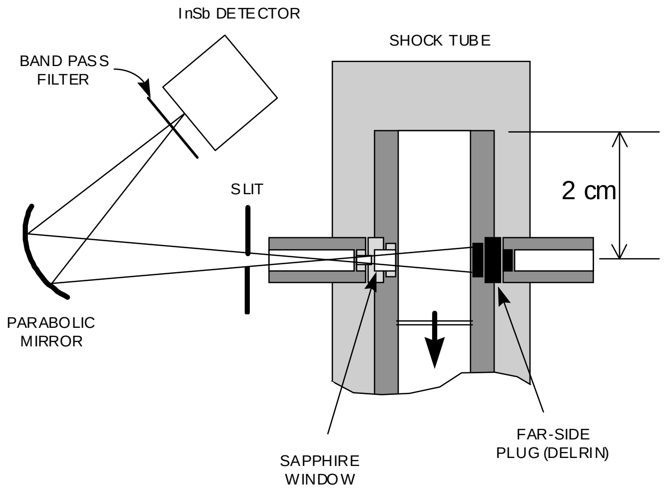

Fig. 2. Infrared emission setup for the Stanford High Pressure Shock Tube (not to scale)

3.2 Measurement procedure

Experiments using the Fig. 2 infrared emission setup were conducted behind reflected shock waves in the HPST to characterize the temperature nonuniformity. Small fractions of CO (500–8000 ppm) were pre-mixed with the argon test gas; at elevated temperatures and pressures, the CO molecules became vibrationally excited and emitted infrared radiation that was detected by the ir-emission setup. A narrow-band filter ($\lambda = 4.181 - 4.742\,\mu\mathrm{m}$, FWHM) was employed to monitor only emission from the CO fundamental vibration centered near $2143\,\mathrm{cm}^{-1}$. To accelerate the relatively slow vibrational relaxation of the CO molecules, small amounts of H_2 were added to the mixtures. All emission measurements were performed 20 mm from the shock-tube endwall.

A 5-cm-dia parabolic mirror with a 15-cm focal length was utilized in the optical setup (Fig. 2). The mirror was located 45 cm from the near inside wall of the shock tube, and the InSb detector (Judson J10D-DB3-1X3M-MTL) was placed 22 cm from the focusing mirror. The slit size was typically 1 mm and was positioned 17 cm from the inside wall of the shock tube, directly external to the retaining stud. A Delrin plug was used in the port directly opposite the sapphire window to minimize the background emission from the shock tube walls. The small, residual background emission (see Petersen, 1998), although characterized for the conditions of the CO-emission tests (Davidson et al., 1998), was not a factor in the relative temperature calculations; no correction to the signals was needed. Similarly, the minor self-absorption observed in the highest CO-concentration mixtures (Davidson et al., 1998) did not influence the ΔT measurements and was therefore ignored in the calculations.

Unshielded pressure measurements were also taken during the ir-emission experiments. However, while the pressure traces exhibited attenuation effects (i.e., an increasing pressure), the results were sensitive to heat transfer from the post-shock gases. As a result, pressure was not used to infer the density changes behind the reflected shock wave for the CO-emission tests herein. Details on the relationship between attenuation effects and the measured pressure are discussed in a later section.

The basis for the temperature measurements is the relationship between the measured ir-emission intensity and the temperature and density of the emitting molecules. Assuming the harmonic oscillator model for the CO vibration (Vincenti and Kruger, 1965), the emission intensity is (Guinee et al., 1980; Hayashi and Goto, 1990; Ciezki and Adomeit, 1990)

$$I = \frac{\beta\,[\mathrm{CO}]}{e^{\theta_v/T} - 1} = \frac{\beta}{e^{\theta_v/T} - 1}\left(\frac{P_{\mathrm{CO}}}{Z R_u T}\right) \qquad (2)$$

where β is the calibration constant of the optical setup, T is the temperature, P_{CO} is the partial pressure of CO, R_u is the universal gas constant, and $\theta_v = \mathrm{h}\nu/\mathrm{k}$. The compressibility, Z, is included because real-gas effects may be important for the shock tube conditions of interest (Davidson and Hanson, 1996). The θ_v constant for CO is equal to 3085 K for the average oscillation frequency, ν, of $2143\,\mathrm{cm}^{-1}$. If the calibration constant β were known, Eq. (2) could be solved for the absolute temperature for a given CO mole fraction, pressure, and emission intensity. However, since the change in temperature was the parameter of primary interest, Eq. (2) was instead differentiated and normalized to the initial conditions. The initial temperature and pressure (T_0 and P_0) were assumed to be the values calculated from the measured incident-shock velocity and the ideal, 1-D theory at the time immediately after shock reflection from the endwall.

Differentiating $I(T, P)$ in Eq. (2) with respect to time, normalizing by the initial values I_0, T_0, Z_0, and P_0, and solving for $\mathrm{d}T/\mathrm{d}t$ results in, for relatively small changes in P and T (i.e., $P \approx P_0$ and $T \approx T_0$)

$$\frac{\mathrm{d}\,(T/T_0)}{\mathrm{d}t} \cong \left[\frac{\mathrm{d}\,(I/I_0)}{\mathrm{d}t} - \frac{\mathrm{d}\,(P/P_0)}{\mathrm{d}t} + \frac{\mathrm{d}\,(Z/Z_0)}{\mathrm{d}t}\right] \times \frac{T_0\left(e^{\theta_v/T_0} - 1\right)}{\left[e^{\theta_v/T_0}\left(\theta_v - T_0\right) + T_0\right]}. \qquad (3)$$

Assuming the relationship between the pressure and temperature is isentropic (i.e., adiabatic and reversible), the isentropic change in pressure can be shown to be

$$\left.\frac{\mathrm{d}P}{\mathrm{d}t}\right|_{\mathrm{isen}} = \frac{P_0}{T_0}\left(\frac{\gamma}{\gamma - 1}\right)\left(\frac{P}{P_0}\right)^{1/\gamma}\frac{\mathrm{d}T}{\mathrm{d}t}. \qquad (4)$$

Combining Eqs. (3) and (4), again invoking the approximation that $P/P_0 \approx 1$ in conjunction with the additional assumption that $\mathrm{d}Z/\mathrm{d}t \approx 0$ (see below), the final expression for the temperature slope as a function of the measured change in ir emission is

$$\frac{\mathrm{d}\,(T/T_0)}{\mathrm{d}t} \cong \frac{B\frac{\mathrm{d}(I/I_0)}{\mathrm{d}t}}{1 + B\frac{\gamma}{(\gamma - 1)}} \qquad (5)$$

where

$$B = \frac{T_0\left(e^{\theta_v/T_0} - 1\right)}{\left[e^{\theta_v/T_0}\left(\theta_v - T_0\right) + T_0\right]}. \qquad (6)$$

By assuming an isentropic relationship between the temperature and pressure, the need for pressure measurements is alleviated. Previous investigators likewise assumed their reflected-shock flow fields were isentropic (Just and Schmalz, 1968; Flower, 1976; Hayashi and Goto, 1990; Ciezki and Adomeit, 1990). Both analytical-model predictions and shielded pressure measurements support the isentropic assumption (see below).

The real gas effects drop out due to the assumption that $\mathrm{d}Z/\mathrm{d}t = 0$. This assumption is valid in the present context because we are only interested in the change in temperature, which is not as sensitive to the small change in Z during an experiment as it is to changes in the pressure. For example, the data of Davidson et al. (1998) indicate that for argon shocks at 500 atm, $\mathrm{d}Z/\mathrm{d}T \approx -4 \times 10^{-5}\,\mathrm{K}^{-1}$, so for a ΔT_5 (after 0.5 ms) as high as 40 K ($T_0 = 1800\,\mathrm{K}$, $P_0 = 500$ atm), Z only changes from 1.075 to 1.072, or about 0.3%. The resulting slope term in Eq. (3), $\mathrm{d}(Z/Z_0)/\mathrm{d}t$, is approximately $5\,\mathrm{s}^{-1}$; this value is 10–20 times smaller than the corresponding pressure slopes (see Table 1 and discussion below) and is therefore neglected herein.

3.3 Carbon monoxide emission measurements

A number of CO infrared emission measurements were performed (mostly in conjunction with other studies (Davidson et al., 1998)) from which the increase in temperature behind the reflected shock wave was inferred. Presented in Table 1 are 73 representative experiments covering reflected-shock temperatures between 1275 and 1900 K and pressures from 24 to 530 atm. Since the percentages of CO and H_2 in the test gas were small (typically $\ll 1\%$), and assuming the CO vibrationally equilibrated to the bath-gas temperature, the ΔT results herein pertain to an ideal, pure-argon driven gas.

A noticeable increase in ir emission at times after passage of the reflected shock wave was observed in each experiment. This trend is evident in the sample emission signal displayed in Fig. 3, normalized to its time-zero value. A common trend in all the experiments was the near-linear behavior of the increasing emission. Hence, the results listed in Table 1 assume constant slopes, normalized to I_0. From the measured $\mathrm{d}I/\mathrm{d}t$, the changes in pressure and temperature could be calculated via Eqs. (4) and (5), respectively. These $\mathrm{d}T/\mathrm{d}t$ and $\mathrm{d}P/\mathrm{d}t$ results (normalized to T_0 and P_0) are also provided in Table 1.

Possibly the most significant result of the temperature-characterization tests is that nonideal-flow effects cause the test temperature to increase with time. Typical ΔT's at 100 and 500 µs (inferred from the ir-emission data) are given in Table 2 for a representative range of pressures and temperatures. The temperature rise at 100 µs can be as high as 8 K, and the temperature increase at 500 µs approaches 40 K or more. In general, the nonideal temperature effects are greatest at lower pressures (where the boundary layer is thicker and the incident-shock attenuation is higher) and higher temperatures. For pressures above 60 atm, the ΔT characteristics are similar.

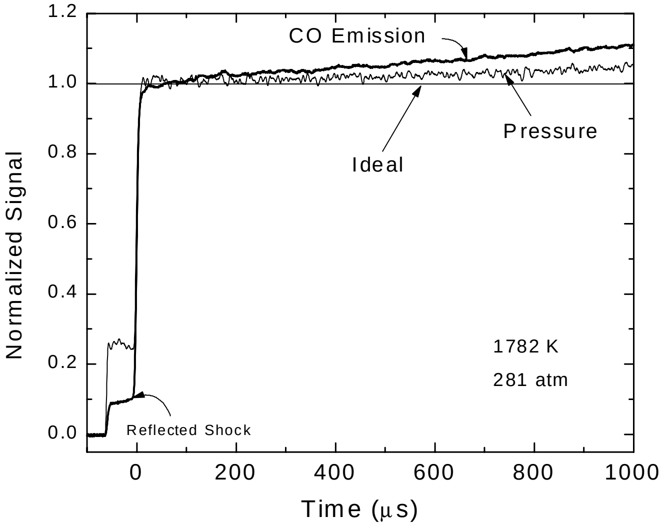

Fig. 3. Sample CO-emission and pressure measurements normalized to their time-zero values. The pressure measurement is from an unshielded PCB 113A transducer. 1782 K, 281 atm, 0.15% CO/0.85% H_2/99% Ar

A primary side effect of the temperature increase is the potential for error in species-concentration and kinetics measurements behind the reflected shock wave. Species mole fractions derived from ir-emission measurements must take into account the change in temperature and pressure with time, and the measurements should be adjusted accordingly. Similar temperature corrections must also be applied to data obtained from other techniques, particularly if the technique is a strong function of temperature. By combining the expected temperature increase with measured emission (or absorption) signals, better interpretation of kinetics data can be made. Further discussion is provided in a later section.

While the measured temperature increase provides useful information on the nonidealities behind the reflected shock wave, CO-emission measurements are not (and cannot be) routinely performed on all experiments. Fortunately, the pressure can be used to infer changes in the test temperature by simply monitoring the change in pressure as a function of time. The resulting $\mathrm{d}T/\mathrm{d}t$ can be inferred directly from Eq. (4) assuming an isentropic relationship between T and P in addition to $P/P_0 \approx 1$. Such a method is convenient since the pressure is monitored on a routine basis, while temperature-measuring techniques such as CO emission cannot be employed on every shock-tube experiment. A fast-response pressure transducer, shielded against heat transfer effects, was proven to be a reliable indication of the reflected-shock nonuniformities (Petersen, 1998).

Figure 4 compares actual $\mathrm{d}P/\mathrm{d}t$ measurements from a shielded pressure transducer to the isentropic assumption, where the agreement is satisfactory. Note that there is considerably more scatter when an unshielded transducer is utilized. The $\mathrm{d}T/\mathrm{d}t$ values plotted on the horizontal axis were obtained from the reflected-shock analytical model, discussed in the following section, for the measured incident-shock attenuation. Calculated $\mathrm{d}T/\mathrm{d}t$

Table 1. Reflected-shock nonuniformity data from CO-emission experiments. The slopes are normalized to their initial values. The * signifies the variable is normalized to its initial, time-zero value. The test temperatures and pressures were calculated from the measured shock velocities assuming the driven gas behaves ideally (i.e., the real-gas effects are secondary when concerned with the nonuniformities due to gas dynamics)

Run	T (K)	P (atm)	Att (%/m)	dI^*/dt (s^{-1})	dP^*/dt (s^{-1})	dT^*/dt (s^{-1})
875	1275	61.1	3.50	144.0	87	35
884	1379	62.3	3.96	151.0	94	38
885	1641	59.2	4.12	173.0	116	47
887	1489	59.2	3.76	160.0	103	41
890	1815	52.8	3.81	137.0	96	38
891	1522	60.4	3.99	132.0	86	34
892	1521	37.7	3.79	126.0	82	33
897	1335	33.4	2.89	143.0	88	35
907	1461	33.1	3.53	187.0	120	48
915	1424	32.1	4.01	171.0	108	43
916	1464	33.7	3.56	186.0	119	48
931	1410	62.9	2.93	125.0	79	32
932	1598	61.1	3.26	135.0	90	36
933	1493	33.6	3.01	144.0	93	37
934	1696	31.8	3.19	170.0	116	46
938	1546	24.8	3.32	154.0	101	40
1075	1431	67.7	3.39	100.2	64	25
1077	1509	61.7	4.06	119.1	77	31
1096	1611	196.7	2.52	85.0	57	23
1097	1586	63.7	3.08	101.2	67	27
1098	1622	199.1	1.93	110.9	74	30
1103	1628	198.8	2.09	109.2	73	29
1104	1460	205.3	1.72	99.4	64	25
1105	1624	166.4	2.32	92.9	62	25
1106	1439	181.3	1.91	86.4	55	22
1131	1445	176.7	1.82	99.2	63	25
1132	1499	173.8	2.18	88.2	57	23
1133	1528	161.4	1.97	81.1	53	21
1149	1803	158.7	2.16	135.2	94	38
1150	1722	159.8	2.14	113.0	77	31
1151	1711	160.8	2.92	114.2	78	31
1174	1452	69.2	2.59	109.5	70	28
1175	1470	70.5	3.02	98.9	64	25
1182	1485	70.7	3.25	94.2	61	24
1183	1642	66.8	2.66	99.7	67	27
1184	1895	63.3	3.35	126.3	90	36
1185	1508	72.6	3.60	94.6	61	25
1187	1443	192.7	1.70	85.3	54	22
1190	1566	69.7	3.91	97.4	64	26
1191	1581	493.3	1.89	92.1	61	24
1193	1492	71.3	3.22	110.4	71	29
1194	1436	69.3	2.52	98.4	63	25
1197	1580	64.3	3.48	114.3	76	30
1198	1803	60.2	3.70	129.3	90	36
1201	1300	166.6	1.93	93.2	57	23
1204	1366	63.0	2.93	94.3	59	23
1206	1469	69.9	3.31	94.7	61	24
1207	1402	65.5	2.15	120.2	76	30
1211	1628	66.4	2.71	148.4	100	40
1214	1399	65.6	2.54	121.4	76	31
1216	1314	168.6	1.20	97.8	60	24
1217	1602	164.0	2.93	100.5	67	27
1218	1748	160.4	2.09	122.0	84	34
1219	1376	63.5	2.68	112.5	70	28
1221	1771	58.3	3.65	164.0	114	45
1222	1389	174.8	2.24	98.0	61	25
1223	1398	90.2	2.27	94.3	59	24
1224	1854	162.1	2.48	134.2	94	38
1228	1541	278.5	1.74	88.7	58	23
1229	1782	280.9	2.40	112.0	78	31
1235	1619	65.5	3.26	128.2	86	34
1236	1536	60.7	3.50	126.9	83	33
1237	1529	302.9	1.91	91.2	60	24
1238	1424	316.7	1.94	85.6	54	22
1239	1374	316.4	1.44	91.2	57	23
1240	1885	270.3	1.56	157.2	111	45
1244	1520	64.0	3.23	130.3	85	34
1245	1489	62.4	2.73	124.0	80	32
1247	1398	510.3	1.26	86.0	54	22
1248	1358	505.4	1.92	106.8	66	26
1250	1713	268.2	2.76	120.8	83	33
1251	1775	520.9	1.76	141.0	98	39
1252	1359	529.1	1.56	74.0	46	18

values are used in Fig. 4 in lieu of measured values because the shielded transducer was, unfortunately, not employed for most of the CO-emission ΔT_5 experiments, as mentioned above; we show below that the reflected-shock model agrees well with available dT/dt measurements and can therefore be used in Fig. 4 without appreciable error.

4 Reflected-shock model

To supplement the experimental characterization and to gain insight into the physics of the nonideal effects, an analytical model was developed. Previous reflected-shock models are reviewed to provide a background into existing

Table 2. Typical inferred temperature and pressure changes at 100 and 500 μs after reflected-shock passage

Run	P_0 (atm)	T_0 (K)	100 μs ΔP (atm)	100 μs ΔT (K)	500 μs ΔP (atm)	500 μs ΔT (K)
915	32.1	1424	0.3	6	1.7	31
934	31.8	1696	0.4	8	1.8	39
1174	69.2	1452	0.5	4	2.4	20
1184	63.3	1895	0.6	7	2.8	34
1222	174.8	1389	1.1	3	5.4	17
1224	162.1	1854	1.5	7	7.6	35
1239	316.4	1374	1.8	3	9.0	16
1240	270.3	1885	3	8	15.0	42
1248	505.4	1358	3.4	4	16.7	18
1251	520.9	1775	5.1	7	25.4	35

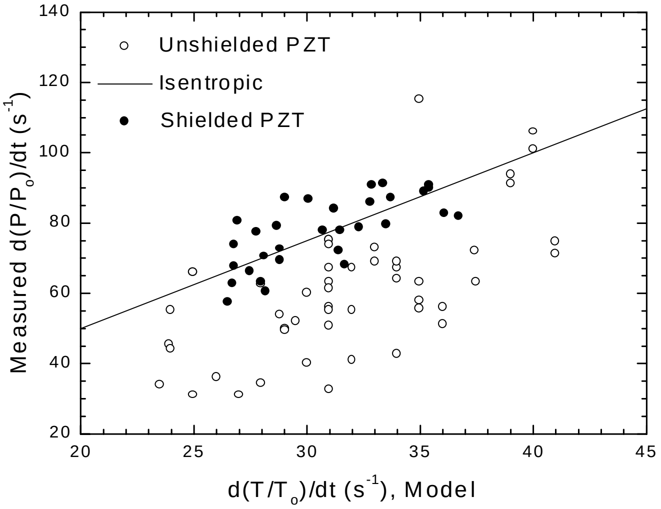

Fig. 4. Measured pressure rise behind reflected shock waves for an unshielded and a shielded pressure transducer. The $\mathrm{d}T/\mathrm{d}t$'s were calculated with the reflected-shock analytical model

theory, followed by a presentation of the theory employed in the present model. Typical results from the theoretical model are then summarized and compared with measurement.

4.1 Background

While predictive models of nonideal behavior behind incident shock waves exist and have been employed to correct chemical kinetics measurements (Warshay, 1968; Belford and Strehlow, 1969; Belles and Brabbs, 1971; Brabbs and Belles, 1972; Bertin et al., 1975; Fujii et al., 1979), comparatively few models are available to calculate nonideal behavior behind the reflected shock wave. Among the first theoretical works to address the reflected-shock/boundary layer interaction and its repercussions on conditions within the reflected region was that of Rudinger (1961). In his study, Rudinger assumed isentropic flow within the reflected- and incident-shock regions and used the theory of Mirels to predict the nonuniform conditions behind the incident shock wave. It was observed that relatively small pressure perturbations behind the incident shock wave are amplified into larger pressure increases behind the reflected shock. In later studies, Hanson (1970; 1971) assumed small perturbations to predict nonuniformities behind the reflected shock caused by the propagation of the reflected wave into a nonuniform flow field. The nonuniform flow behind the incident wave was defined by a known incident-shock axial Mach number profile, and the simplified theory agreed well with a more-extensive, method of characteristics model.

One of the only theoretical works to address the effect of reflected-shock nonuniformities on chemical kinetic measurements is that of Michael and Sutherland (1986). In their paper, theory was compared to pressure and velocity measurements to develop a method for correcting the measured kinetics data for temperature and pressure perturbations, assuming isentropic flow within the reflected-shock region. Kinetics measurements in reflected shock waves at low Mach numbers using the correction method of Michael and Sutherland were presented in a later study (Michael and Fisher, 1990). The boundary-layer corrections led to lower rate coefficients and higher activation energies than those determined from ideal shock tube theory.

4.2 Theory

A reflected shock wave model was developed to estimate the nonuniformities attributed to the nonideal effects discussed above. The conditions into which the reflected shock wave travels are determined using the turbulent boundary layer and attenuation procedures presented by Mirels (1963; 1964) and Petersen (1998). In general, the reflected-shock model is similar to the one used by Rudinger (1961) for a low-pressure shock tube, the primary exceptions being the improved turbulent friction model (Petersen, 1998) and the use of measured/defined incident-shock velocity profiles as in Hanson (1970; 1971). By prescribing the shock trajectory in addition to the incident-flow nonuniformity, the nonideal effects due to both friction and diaphragm breakage are accounted for. The resulting effects on the conditions in the reflected-shock region at the measurement location are calculated using the techniques laid out in Rudinger (1969). The basic theory and model development are as follows.

A schematic diagram of the reflected-shock process is given in Fig. 5. Point A represents the measurement/test location in the shock tube. The lines CA and FD represent right-running characteristic waves, and DA a left-running wave, through which information in the form of pressure waves travels from the endwall and the region immediately behind the reflected shock wave to the test section. Therefore, disturbances due to nonuniform conditions upstream of the reflected shock wave can influence the pressure and temperature at point A. Lines CA and FD are defined as P-waves, and line DA represents a Q-wave.

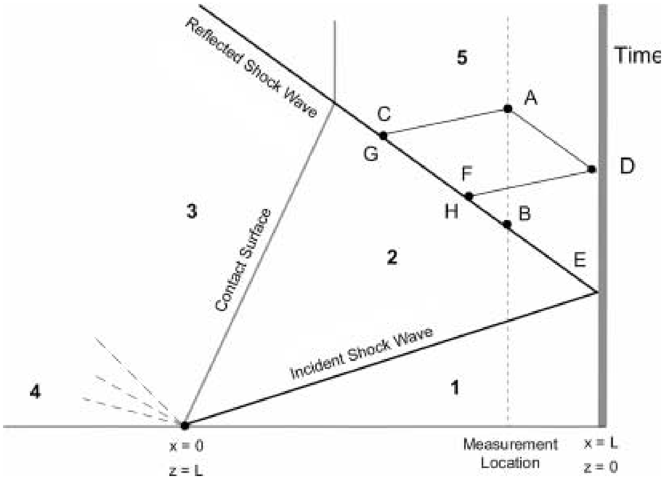

Fig. 5. $x - t$ diagram for reflected shock wave

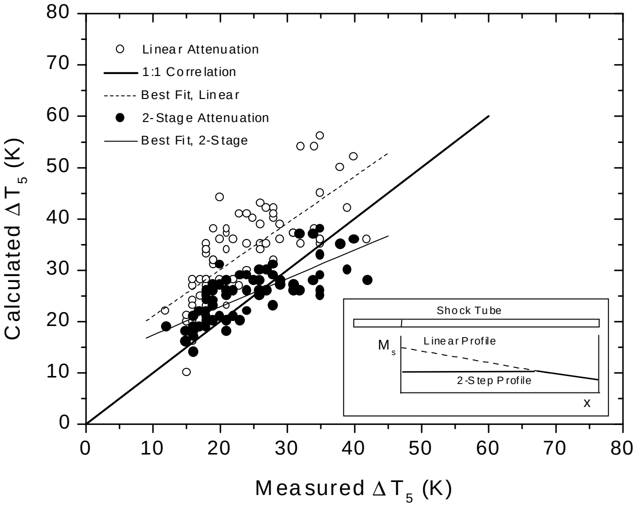

Fig. 6. Comparison between measured ΔT_5 at 500 µs and calculated ΔT_5 using the reflected-shock model described herein. Two assumptions for the M_s profile are provided

As discussed in Rudinger (1969), it is convenient to define the Riemann variables for the P and Q waves as

$$P = \frac{2}{(\gamma - 1)} a + u \tag{7}$$

$$Q = \frac{2}{(\gamma - 1)} a - u \tag{8}$$

where γ is the specific heat ratio, a is the sound speed $(\gamma RT)^{1/2}$, and u is the bulk fluid velocity in the x direction. Upon solution of the continuity and momentum equations, it can be shown that the P and Q characteristic waves are related to the entropy via

$$\frac{\partial P}{\partial t} + (a + u)\frac{\partial P}{\partial x} = a\left[\gamma \frac{\partial S}{\partial t} + (a + \gamma u)\frac{\partial S}{\partial x}\right] \tag{9}$$

$$\frac{\partial Q}{\partial t} + (a - u)\frac{\partial Q}{\partial x} = a\left[\gamma \frac{\partial S}{\partial t} + (a - \gamma u)\frac{\partial S}{\partial x}\right]. \tag{10}$$

The normalized entropy, S, is defined relative to the initial conditions in region 1 as follows:

$$S = \frac{s - s_1}{c_p(\gamma - 1)} = \frac{1}{(\gamma - 1)} \ln(T/T_1) - \frac{1}{\gamma} \ln(P/P_1) \tag{11}$$

where s is the entropy, c_p is the constant-pressure specific heat and, of course, the P in Eq. (11) is the pressure and not the Riemann variable.

Equations (7) through (11) are combined with the definition of the sound speed in a perfect gas to solve for the conditions at point A as a function of time, remembering that Eqs. (9) and (10) only apply along the waves defined in Fig. 5. In the solution procedure, the conditions at points C and F are obtained from the normal-shock relations while the conditions at points G and H, respectively, are calculated using the incident-shock/boundary layer techniques outlined in Petersen (1998) and Mirels (1963; 1964). The conditions immediately downstream of the reflected shock wave are given relative to the upstream conditions by the classical 1-D, normal-shock relations (Gaydon and Hurle, 1963). The trajectory of the reflected shock wave must be provided. In the present model, the reflected-shock velocity w_R is assumed to be constant and equal to the lab-frame velocity defined at point E. (The conditions at point E are known from the measured incident-shock trajectory and the initial driven-gas conditions.)

A further assumption is that the flow is adiabatic, implying that each mass particle behaves isentropically. Since the flow within region 5 is virtually stagnant, the particle paths are nearly vertical lines on an $x - t$ diagram. The entropy at point A, therefore, remains the same as that at point B (which is known). This multi-isentropic assumption and the assumption that the bulk flow velocity is negligible were confirmed in separate calculations. This greatly simplifies the solution of Eqs. (9) and (10), wherein the CA, DA, and FD characteristics lead to $P_A = P_C$, $Q_A = Q_D$, and $Q_D = P_D = P_F$ (since $u_D = 0$ from the wall boundary condition). Therefore, u_A, T_A, and T_D can be found by repeated application of the Riemann relations (Eqs. (7) and (8)) and the speed of sound. Equation (11) is then used to obtain the pressure at point A since S_A is approximately constant. In all cases, u_A was found to be less than 1% of the reflected-shock velocity, supporting the $S_A = S_B$ assumption.

As mentioned above, the incident Mach number must be provided as a function of axial distance. In most attenuation models such as Mirels (1963, 1964), the axial shock profile is assumed to vary linearly from its maximum value at the diaphragm to its minimum value at the endwall. However, the linear assumption tended to over predict the change in T_5 for the conditions herein (where the measured attenuation at the endwall was extrapolated linearly back to the diaphragm). Since the shock velocity was only measured in the HPST over approximately the last meter (out of a 5-m total length), the entire Mach

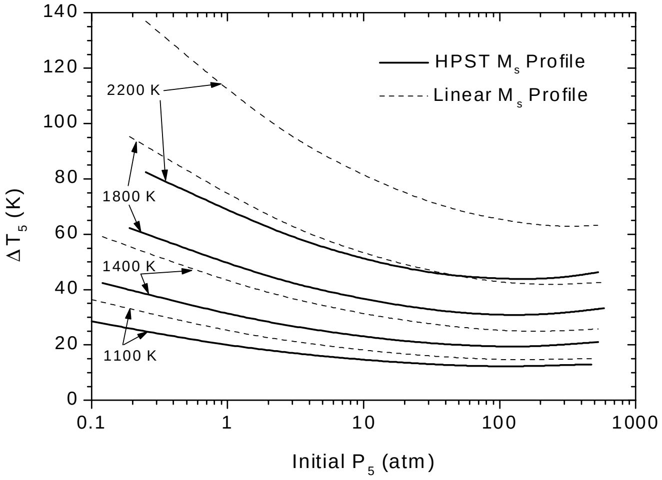

Fig. 7. Effect of pressure and temperature on temperature increase at $t = 500\,\mu s$ behind the reflected shock wave in the HPST (in argon). All values shown were calculated using the reflected-shock model along with a realistic estimate of the attenuation using Eq. (1)

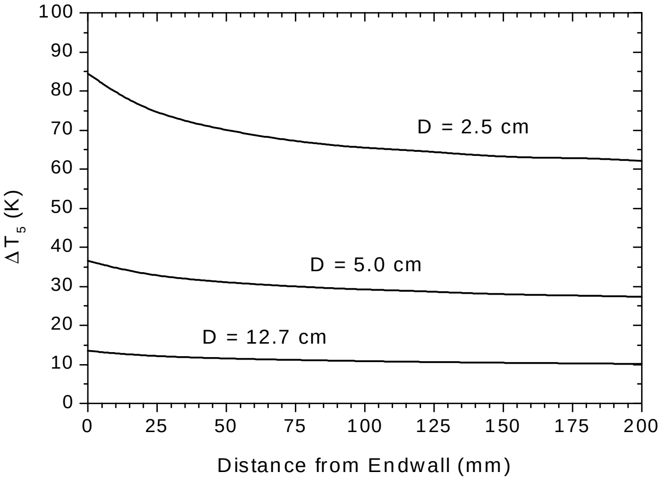

Fig. 8. Effect of shock tube diameter and test section location on the temperature increase behind the reflected shock wave at $t = 500\,\mu s$. All values were calculated using the reflected-shock model along with the incident-shock model's (Petersen, 1998) estimate of the attenuation (including viscous effects only). $T_0 = 1800\,K$, $P_0 = 100\,atm$, argon

number profile was not known. A 2-stage profile wherein M_s is constant over the first 4 meters and varies over the last meter per the measured attenuation rate led to better agreement between model and experiment (see imbedded schematic in Fig. 6). Typical results from the two M_s-profile assumptions are provided in the following section.

4.3 Model results

The reflected-shock model was validated by comparing the predicted temperature (and pressure) rise with the measured values from the CO-emission experiments. Table 3 lists the predicted and measured ΔT_5 at $t = 500\,\mu s$ for a representative range of data from the original Table 1 compilation, and Fig. 6 presents a comparison between theory and experiment for the two Mach number-profile assumptions. The model predictions using a linear M_s variation are higher than the measured ΔT_5, while the 2-stage attenuation model provides better agreement. The results of the 2-stage model are not surprising since measurements of axial M_s values by other investigators indicate a near-parabolic profile (e.g., Simpson et al., 1967). Further experiments with additional velocity-measurement locations are required to obtain the complete M_s profile over the entire 5-m driven section of the Stanford HPST.

Nonetheless, the model compares well with experiment, and the calculated temperature rise is, in general, within 5 K for a wide range of incident-shock attenuation (1.5–4.0%/m) and Mach number (2.2–2.6). The few examples where the disagreement is 5 K or more are, however, not surprising and can be attributed to the uncertainty and variation in the attenuation, as seen in Fig. 1, and to the uncertainties in defining a $\mathrm{d}I/\mathrm{d}t$ from the CO-emission measurements.

Because of the good agreement between model and experiment, the theoretical model can be utilized to estimate trends as a function of certain shock-tube parameters and test conditions. For example, the effects of test pressure and temperature on the temperature increase were evaluated over a range of P_5 and T_5; realistic attenuation rates using the attenuation correlation of Eq. (1) were utilized. Figure 7 displays ΔT_5 results at $t = 500\,\mu s$ for a pure argon test gas at pressures between 0.1 and 500 atm and temperatures of 1100, 1400, 1800, and 2200 K. Calculations using both Mach number assumptions are provided, where the 2-stage model is also referred to as the HPST M_s profile because of its good agreement with the data (Fig. 6).

As pressure increases, the temperature change decreases. For example, the ΔT_5 at 1800 K, 100 atm is nearly 20 K lower than at 1800 K, 1 atm, and there is little difference in the temperature change between 100 and 500 atm. In contrast, the test temperature has a marked effect on the nonideal gas dynamics, where the 500-μs temperature increase can be 40 K higher at 2200 K ($\Delta T = 45$ to 85 K) than at 1400 K ($\Delta T = 20$ to 45 K).

In summary, nonideal gas dynamics behind the reflected shock wave are worse at lower pressures and higher temperatures. These trends are due primarily to the increased turbulent boundary layer thickness at lower pressures and higher incident shock wave speeds (i.e., higher test temperatures) (Petersen, 1998). The experimental data in Table 2, the attenuation data in Fig. 1, and the Eq. (1) attenuation expression support the Fig. 7 trends.

Although the HPST dimensions are fixed, a useful application of the reflected-shock model is to determine what effects shock tube diameter and test-section location have on nonideal gas dynamics. Presented in Fig. 8 is a comparison of the ΔT_5 at 500 μs for three shock tube diameters: 2.5, 5.0, and 12.7 cm (1, 2, and 5 inches, respectively) over a range of positions relative to the endwall ($z = 0$ to 200 mm). For the Fig. 8 calculations, the Mach number

Table 3. Comparison between calculated and measured temperature increase at 500 µs after arrival of the reflected shock wave for two assumptions of the incident-shock profile (See Fig. 6)

Run	ΔT at 500 μs (K)			Run	ΔT at 500 μs (K)		
	Meas	Model			Meas	Model	
		Linear Atten	2-Stage Atten			Linear Atten	2-Stage Atten
875	22	28	21	1187	16	23	18
884	26	35	26	1190	20	44	31
885	38	50	35	1191	19	32	26
887	31	37	26	1193	21	34	25
890	35	56	38	1194	18	28	21
891	26	43	30	1197	24	41	29
892	25	40	28	1198	32	54	37
897	23	27	20	1201	15	20	16
907	35	35	25	1204	16	28	21
915	31	37	27	1206	18	34	25
916	35	36	26	1207	21	23	18
931	22	28	21	1211	32	35	26
932	29	39	28	1214	21	26	20
933	28	32	23	1216	16	16	14
934	39	42	30	1217	21	38	28
938	31	37	27	1218	29	36	27
1075	18	33	24	1219	19	27	20
1077	23	41	29	1221	40	52	36
1096	18	35	26	1222	17	25	19
1097	21	37	26	1223	17	25	19
1098	24	35	26	1224	35	45	33
1103	24	35	26	1228	18	27	21
1104	19	31	23	1229	28	42	31
1105	20	36	27	1235	28	40	29
1106	16	24	19	1236	26	39	28
1131	18	23	19	1237	18	28	22
1132	17	28	22	1238	15	10	16
1133	16	27	21	1239	16	20	17
1149	34	38	28	1240	42	36	28
1150	27	35	26	1244	26	34	25
1151	27	42	30	1245	24	30	22
1174	20	28	21	1247	15	21	18
1175	19	32	24	1248	18	22	20
1182	18	34	25	1250	28	41	31
1183	22	36	26	1251	35	36	29
1184	34	54	37	1252	12	22	19
1185	19	38	27				

and P_1 corresponding to a test temperature and pressure of 1800 K and 100 atm, respectively, were used, and a 5-m driven-section length was assumed. Only a linear M_s profile was used since the 2-stage profile that works for the HPST cannot be assumed to work for other shock tubes; the attenuation rate at the endwall was determined using the incident-shock model (Petersen, 1998) prediction without diaphragm-breakage effects.

The impact of test section location is minimal (< 10 K), while the shock tube diameter has a dramatic effect on the temperature increase. For the 2.5-cm tube, the temperature increase at 25 mm, 500 µs (75 K) is over five times greater than the predicted increase for the larger, 12.7-cm tube (14 K). Hence, as expected, smaller shock tube diameters produce greater nonuniformities because the turbulent boundary layer comprises a greater fraction of the total flow area.

It should be noted that the curves in Figs. 7 and 8 required incident-shock attenuation values; these axial velocity profiles were obtained using the incident-shock attenuation code discussed in Petersen (1998) and, thus, include only the effects of friction. The actual 500-µs ΔT's for the HPST would be approximately 5 K higher than those in Figs. 7 and 8 due to additional diaphragm-breakage nonidealities. Nonetheless, the results in Figs. 7 and 8 display the correct trends and are representative of the relative effect that P_5 and T_5 have on the reflected-shock nonuniformities. Since the primary function of the gas dynamic routine described herein is the estimation of reflected-shock nonuniformities for a given attenuation and Mach number, which are measured on every experiment, an *a priori* prediction of the attenuation including both friction and nonideal diaphragm rupture is not needed. The nonideal diaphragm contribution to the attenuation can, of course, be estimated using the friction model and the HPST data in Fig. 1 (and Eq. (1)), but the results would only apply to the HPST. The diaphragm effects would differ from shock tube to shock tube while the viscous prediction utilizes a more general procedure.

As demonstrated in the following section, the analytical model can be used to predict the attenuation-induced temperature and pressure increase for any shock-tube experiment wherein the axial shock velocity profile is measured. This is the application where the analytical model is most useful because the corrected temperature and pressure can be incorporated into the data reduction process. The effect on shock tube chemistry can then be evaluated.

5 Discussion

According to the experimental results and the analytical model, the temperature increase behind the reflected shock wave approaches 30 K or more after 500 µs. Such a temperature increase can influence the interpretation of laser absorption- and infrared emission-based species profiles, thus impacting kinetics analysis and data reduction. In this section, sample calculations are utilized to demonstrate the repercussions that nonuniform temperature and pressure have on chemistry experiments. The effects on chemical kinetic calculations are described first, where an indication of the proper analysis techniques and the trends one might expect to see are provided. Species-profile measurements are discussed next, and specific examples employing absorbing molecules of interest in the laboratory are reviewed

5.1 Kinetics calculations

Typically, shock-tube chemical kinetics measurements are performed with a test gas composed of a minor constituent mixed with a bath gas such as argon or nitrogen. The large diluent fraction (usually $> 97\%$) serves as the primary third-body, but it also plays the role as a heat sink that minimizes reaction-related temperature changes. In essence, shock tube experiments are designed to provide the conditions of a premixed, constant-temperature and -pressure reactor. However, temperature and pressure changes resulting from a temporally non-uniform post-shock flow field can negate the usual assumption that changes in the reaction temperature and pressure are negligible. The impact of flow non-uniformities on the chemical kinetics must be evaluated and, in certain cases, compensated for.

The effect of increasing temperature and pressure can be determined analytically using Chemkin II (Kee et al., 1989) by specifying T and P as a function of time *a priori*. This option of Chemkin is in lieu of using the constant–h, P or constant–u, V options, and, of course, assumes that the temperature and pressure increase due to reaction is negligible. To demonstrate, a stoichiometric mixture of 1000 ppm H_2, 500 ppm O_2, balance argon was utilized in the calculations, and the $\mathrm{d}P/\mathrm{d}t$ and $\mathrm{d}T/\mathrm{d}t$ values were obtained via the incident- and reflected-shock models. An initial reflected-shock pressure of 65 atm was assumed, and two temperatures were selected (1550 and 1350 K), representing fast and slow chemistry. The detailed kinetics mechanism was taken from the $H_2{-}O_2$ subset of the GRI-Mech 1.2 mechanism (Frenklach et al., 1995). Since hydroxyl-radical formation and depletion give a good indication of ignition time and peak mole fraction, OH mole fraction was utilized as the primary Chemkin output.

A total test time of 1 ms is utilized in the calculations below. A test of this duration is realistic in the Stanford HPST since nonideal effects due to contact-surface/reflected-shock interaction, contact-surface arrival, or expansion-wave arrival have been found to occur, typically, at times greater than 1 ms after shock reflection. Figure 3 bears witness to this fact since no disturbances are seen in the pressure or ir emission (and, hence, temperature) traces for post-reflection times as long as 1000 µs.

Figure 9 presents the results of the kinetics model assuming 1) a constant reaction temperature and pressure, and 2) a pressure and temperature increase predicted using the analytical reflected-shock model. The 1550-K results are shown in Fig. 9a, corresponding to $\mathrm{d}(T/T_0)/\mathrm{d}t = 27.6\,\mathrm{s}^{-1}$ and $\mathrm{d}(P/P_0)/\mathrm{d}t = 69.6\,\mathrm{s}^{-1}$ ($\approx 3\%/\mathrm{m}$ incident-shock-speed attenuation). At this higher temperature, the kinetics are fast and reaction occurs shortly after 50 µs,

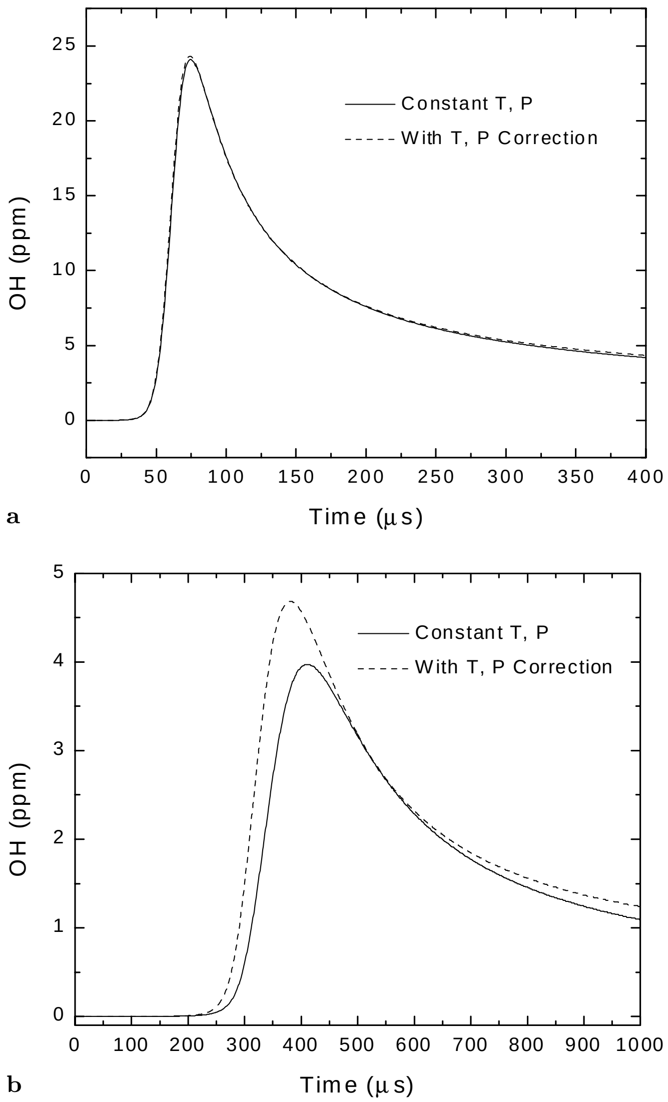

Fig. 9a,b. Predicted OH mole fraction in the HPST assuming: 1) constant T_0 and P_0, and 2) T_0 and P_0 as predicted by reflected-shock model. 1000 ppm H_2, 500 ppm O_2, balance argon. **a** 1550 K, 65 atm (fast kinetics); **b** 1350 K, 65 atm (slow kinetics)

evident by the sharp rise in OH. The attenuation-induced temperature increase at the time of reaction is less than 3 K, so the difference between the attenuation-corrected case and the constant-temperature one is insignificant. Key features such as ignition delay time and peak OH mole fraction would be well within experimental error for this 1550-K case.

Discrepancies, however, become more pronounced at 1350 K, where the ignition delay time is longer. Figure 9b presents the 1350-K comparison, corresponding to a $\mathrm{d}(T/T_0)/\mathrm{d}t$ and a $\mathrm{d}(P/P_0)/\mathrm{d}t$ of 25.5 and 64.2 s^{-1}, respectively. The ignition time for the constant-temperature case is near 400 µs, in contrast to the attenuation-corrected result that has a reaction time that is 35 µs shorter (9% error). In addition, the peak OH mole fraction is greater when nonideal effects are included, primarily because the temperature increases by 15 K prior to ignition (for an average temperature of 1358 K). Similarly, the radical-decay characteristics are different at longer times.

The results displayed in Fig. 9 are representative of the effects nonuniform reflected-shock conditions have on chemical kinetics. In summary, reactions that occur within the first few hundred microseconds are not impacted as much as reactions that extend to longer times. Therefore, the effects of the temperature increase can be minimized via proper experimental design by choosing mixtures and conditions wherein the important kinetics occur at early times. Alternatively, the temperature increase can be inferred from the reflected-shock model, described herein (using the measured attenuation and M_s); using this temperature change, the kinetics analysis of the experimental data can be corrected for the nonuniform conditions.

Unfortunately, the specified (T, P) option in Chemkin and the prediction of energy release due to reaction are mutually exclusive. Unless a model exists that integrates the kinetics with the energy changes behind the reflected shock wave, gas dynamic corrections should only be made when the ΔT due to attenuation overshadows the ΔT expected from exothermic reactions. Such a model would simply have to combine the energy release due to the kinetics with the time-dependent gas dynamics.

5.2 Species profile measurements

While the nonuniform temperature and pressure behind the reflected shock wave impact the chemical kinetics, they can also impact the data reduction process. In cw laser-absorption measurements, the absorption cross section of the absorbing molecule is often temperature-dependent, and pressure broadening and shift often affect the frequency-dependent lineshape function. Therefore, changes in the temperature and pressure during the course of an experiment can affect the interpretation of absorption data via the absorption coefficient and the pressure term in Beer's Law. To gauge the magnitude of the effect, two common shock-tube absorbing molecules with different temperature and pressure sensitivities are discussed: OH and CH_3. In ir-emission measurements, the data are quite sensitive to temperature changes, as seen in the CO measurements above and briefly described below.

5.2.1 OH absorption

The OH molecule is an important chain-branching radical in most combustion systems, particularly in oxidative environments wherein hydrogen and/or hydrocarbons are the fuel. Since its development by Rea et al. (1984) and Rea (1991), cw ring-dye laser absorption monitoring of OH has been a primary shock tube diagnostic in low-pressure shock tubes and, more recently, in the High Pressure Shock Tube (Davidson et al., 1996). As summarized by Rea et al. (1984), the OH absorption coefficient depends on the collision width and collision shift, both of

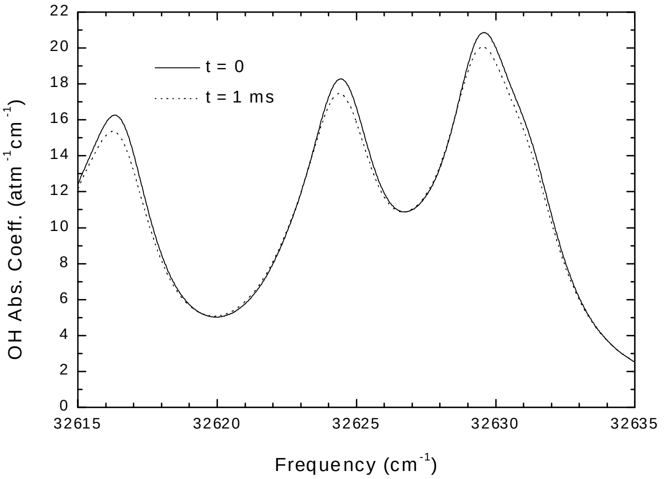

Fig. 10. OH absorption coefficient for A–X (0,0) 306-nm Bandhead at $t = 0$ and $t = 1\,\mathrm{ms}$ after passage of the reflected shock wave (including the temperature and pressure increase predicted by the reflected-shock gas dynamic model). $T_0 = 1350\,\mathrm{K}$, $P_0 = 65\,\mathrm{atm}$; T (1 ms) = 1384 K, P(1 ms)= 69.2 atm. Calculated per Davidson et al. (1996)

which exhibit temperature and pressure dependence. In Davidson et al. (1996), the broadening and shift of the OH A–X (0,0) bandhead near 306 nm was characterized at high pressure and temperature (60 atm, 1735 K) in argon. The 306-nm laser light was accessed via a cw ring-dye laser operating at 612 nm, frequency-doubled using an intra-cavity AD*A crystal. The measured collision width, $\Delta\nu_{\mathrm{width}}$, at elevated pressure was found to vary with temperature and pressure as follows:

$$\Delta\nu_{\mathrm{width}} \propto PT^{-0.75}\,. \tag{12}$$

The shift, $\Delta\nu_{\mathrm{shift}}$, is similarly dependent on T and P:

$$\Delta\nu_{\mathrm{shift}} \propto -PT^{-0.45}\,. \tag{13}$$

Changes in temperature and pressure during the course of an experiment can affect the spectral absorption coefficient, and hence the OH mole fraction, via the T and P dependencies in Eqs. (12) and (13).

Using typical HPST values for ΔT_5 and ΔP_5, and a specified mixture with known kinetics, the change in absorption coefficient and, hence, the change in the percent absorption of the laser light can be predicted analytically. (This situation is simply the inverse of what normally occurs during an experiment, where the percent absorption is measured and the mole fraction is inferred from Beer's Law.) For example, assuming OH is produced in a mixture of 0.1% H_2, 0.05% O_2 in argon, shock heated initially to 65 atm and 1350 K, the temperature and pressure after 1 ms would increase to 1384 K and 69.2 atm ($\Delta T = 34\,\mathrm{K}$, $\Delta P = 4.2\,\mathrm{atm}$).

A comparison of the OH A–X (0,0) band at $t = 0$ and $t = 1\,\mathrm{ms}$ is provided in Fig. 10, calculated per Davidson et al. (1996). There is little difference between the two spectra at the key frequency of 32630 cm^{-1}. The corresponding OH profiles (at 32630 cm^{-1}), calculated using Chemkin, the GRI-Mech 1.2 mechanism, and Beer's Law, are presented in Fig. 11. The difference between the $t = 0$ and $t = 1\,\mathrm{ms}$ profiles is less than 0.1%, which is well within the accuracy of the laser absorption technique in the High Pressure Shock Tube.

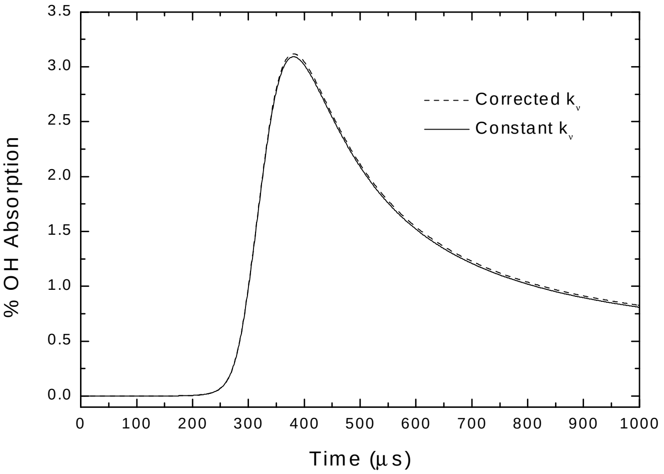

Fig. 11. OH absorption profiles calculated assuming: 1) a constant absorption coefficient and, 2) one which changes per the calculated T_0 and P_0 increase. Initial conditions are 1350 K and 65 atm, 1000 ppm H_2 + 500 ppm O_2, balance argon; T(1 ms) = 1384 K, P(1 ms) = 69.2 atm

The results of Fig. 11 indicate that the attenuation effects should not have a large impact on the interpretation of OH profiles obtained using laser absorption near 306 nm. The actual $k\nu$ at 32630 cm^{-1} varies only from 20.0 atm^{-1}cm^{-1} at time zero to 19.2 after 1 ms for the conditions of Fig. 11, and the effects of the decreasing absorption coefficient are offset by the increasing pressure in the Beer's Law exponent. This outcome is coupled with the fact that most measurements should be complete long before 1 ms is reached, preferably within the first few hundred microseconds as discussed above. Therefore, for the majority of HPST experiments, a single OH absorption coefficient (defined at T_0 and P_0) and the initial pressure can be utilized in the Beer's Law conversion of raw data from percent absorption to mole fraction. Of course, this assumption can be easily verified for each set of experiments using the procedure outlined above.

5.2.2 Methyl absorption

Another key combustion radical and shock tube diagnostic is CH_3. The primary wavelength of interest is 216.615 nm, corresponding to the Hertzberg β_1 band at high temperature (Davidson et al., 1993). Assuming the pressure dependence at HPST conditions is small, the absorption coefficient of methyl at 216.615 nm given by Davidson et al. (1993) is assumed herein to be valid at elevated pressures:

$$k_{\lambda_{\mathrm{CH_3}}} = (562,400/T)\exp\left(-T/1087\right) \tag{14}$$

where k_λ is the spectral absorption coefficient (atm^{-1}cm^{-1}) and T is the temperature in K. Equation (14) was used to

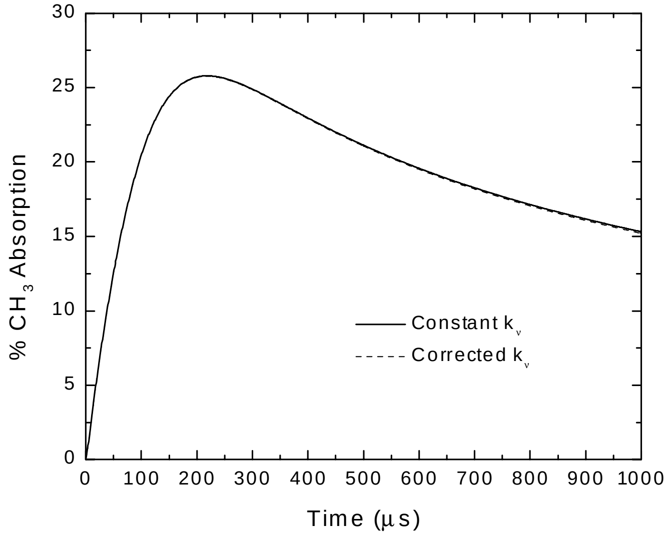

Fig. 12. Calculated CH_3 absorption profiles for: 1) a constant absorption coefficient and, 2) one which changes per the calculated T_5 and P_5 increase. Initial conditions are 1800 K and 100 atm, 100 ppm CH_4, balance argon; $T(1\,\text{ms}) = 1854\,\text{K}$, $P(1\,\text{ms}) = 107.7\,\text{atm}$

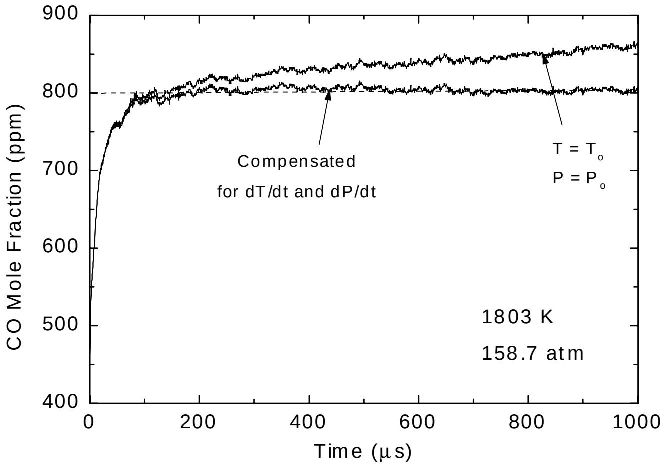

Fig. 13. CO mole fraction inferred from a measurement of CO emission near 4.7 μm; 0.08% CO +0.15% H_2 + Ar; 1803 K, 159 atm. T_5 and P_5 after 1 ms are 1871 K and 174 atm, respectively. The upper curve is uncompensated and therefore includes the effects of the changing T_5 and P_5. By accounting for ΔT_5 and ΔP_5, the inferred mole fraction is constant in the lower curve, as expected

estimate the effect of reflected-shock nonuniformities on the interpretation of CH_3 absorption data in the HPST.

The formation and depletion of methyl was calculated using GRI-Mech 1.2 to model the decomposition of 100-ppm CH_4 in argon, and the initial conditions downstream of the reflected shock wave were assumed to be 1800 K and 100 atm. A temperature increase of $\mathrm{d}(T/T_0)/\mathrm{d}t = 30.5\,\mathrm{s}^{-1}$ and a pressure increase of $\mathrm{d}(P/P_0)/\mathrm{d}t = 70\,\mathrm{s}^{-1}$ were calculated for these specific conditions; this corresponds to a temperature of 1854 K and a pressure of 107.7 atm 1 ms after shock arrival ($\Delta T = 54\,\text{K}$, $\Delta P = 7.7\,\text{atm}$). The absorption coefficient calculated with Eq. (14) is $59.6\,\text{atm}^{-1}\text{cm}^{-1}$ at $t = 0$ and decreases to $55.1\,\text{atm}^{-1}\text{cm}^{-1}$ after one millisecond. Figure 12 shows the calculated CH_3 absorption assuming: 1) a constant T and P equal to the initial values, and 2) an increasing T and P per the calculated nonuniformity. Both CH_3 profiles are virtually identical, as seen in Fig. 11 for OH, i.e., the increasing pressure offsets the decreasing absorption coefficient.

The results of Fig. 12 indicate HPST attenuation does not have a significant impact on conversions between CH_3 absorption profiles and CH_3 mole fraction profiles, and a single $k\nu$ defined at the initial T_5 and P_5 should be adequate for laser absorption measurements near 216 nm.

5.2.3 Infrared emission

Unlike the interpretation of the absorption data, the increasing temperature and pressure behind the reflected shock wave can significantly affect the ir-emission data. According to harmonic oscillator theory, the measured infrared emission from a vibrating molecule depends on the temperature and pressure according to (Vincenti and Kruger, 1965)

$$I \propto \frac{P/T}{\exp\left(\theta_v/T\right) - 1}\,. \tag{15}$$

Hence, the emission signal is sensitive to changes in the test temperature and pressure on the order of the nonideal effects behind the reflected shock wave. Figure 13 presents two X_{CO} plots as inferred from a CO-emission trace (via Eq. (2)) for a 0.08% CO/0.15% H_2/99.77% Ar mixture with an initial T_5 and P_5 of 1803 K and 159 atm. The top plot is uncorrected for the changing T_5 and P_5, while the lower curve includes the appropriate T_5 and P_5 changes using Eqs. (4), (5), and (6). The interpretation error for the uncompensated CO-emission trace would be appreciable, but adjustment of the signal to account for the increasing T and P brings the inferred CO mole fraction to a straight line, as expected since the CO does not decompose at 1803 K. Similar compensation should also be done when analyzing ir emission data from other molecules such as CH_4 and N_2O. When the mole fraction of the emitting species is not known, the measured $\mathrm{d}P/\mathrm{d}t$ can be used to infer the correct I and T correction via Eqs. (4), (5), and (6).

6 Summary

Experiments and calculations related to the measurement and prediction of nonideal gas dynamic effects in the Stanford High Pressure Shock Tube were presented. Because of its importance in chemical kinetic measurements, changes in the test temperature behind the reflected shock wave were highlighted. The change in temperature at a location 2 cm from the endwall was characterized experimentally using an ir-emission technique. Emission from trace levels of CO was used to infer dT/dt, assuming an isentropic relationship between the test temperature and pressure, over a representative range of conditions in argon (24–530 atm, 1275–1900 K). Typically, the temperature increased 3–8 K after 100 µs and 15–40 K after 500 µs, corresponding to near-linear (normalized) temperature and pressure slopes. Separate experiments with a shielded pressure transducer minimized heat transfer effects to the gauge, leading to dP/dt measurements that support the isentropic relationship between pressure and temperature. The change in test temperature can thus be inferred from routine measurements of dP/dt using a shielded pressure transducer since the relationship between T and P is nearly isentropic.

An analytical model was presented that reproduces the nonideal gas dynamics behind the reflected shock wave. The nonuniform conditions upstream of the reflected shock wave were defined using the incident-shock attenuation theory of Petersen (1998) and Mirels (1963; 1964), and the perturbations between the reflected shock wave and the endwall were assumed to propagate along right- and left-running characteristics. The results of the model agree well with experiment; the calculated post-shock ΔT's are, in general, within a few K of the temperature increases obtained with the CO-emission technique. In general, the nonideal effects are greatest at lower pressures and higher temperatures. Since the temperature increase cannot realistically be measured during every experiment, the reflected-shock model can be used, with confidence, in predicting the nonideal conditions behind the reflected shock wave.

In the final section, the effects of increasing test temperature and pressure on chemistry measurements in the HPST were evaluated. Calculations using a chemical kinetics model of H_2–O_2 combustion demonstrated that a positive dT/dt influences the chemistry to a greater extent when the reaction times are longer than approximately 300–500 µs. Therefore, proper experimental design should focus on reactions that occur within the first few hundred microseconds. If nonideal effects cannot be avoided, the accompanying kinetics analysis using a detailed mechanism can be performed for a specified dT/dt and dP/dt prior to comparison with the nonideal data. Separate calculations indicate the reduction of laser absorption data for at least two key species, OH (306 nm) and CH_3 (216 nm), requires little, if any, correction for the changing absorption coefficient since the impact on the mole fraction inferred from Beer's Law is minimal. In contrast, species profiles obtained via ir emission are much more sensitive to changes in T and P, so the data should be compensated accordingly.

Acknowledgements. The Department of Energy, the Office of Naval Research, and the Army Research Office supported the work at Stanford University. The authors wish to thank Dr. David Davidson and Ronald Bates (Stanford) for assistance on the shock tube experiments and John Herbon (Stanford) for reviewing the manuscript and calculations. The preparation of this manuscript and the theoretical calculations were performed at The Aerospace Corporation for The Air Force Space and Missiles System Center under Contract No. F04701-93-C-0094.

References

Belford RL, Strehlow RA (1969) Shock Tube Technique in Chemical Kinetics. Ann. Rev. Phys. Chem. 20: 247

Belles FE, Brabbs TA (1971) Experimental Verification of Effects of Turbulent Boundary Layers on Chemical-Kinetic Measurements in a Shock Tube. In: Thirteenth Symposium (International) on Combustion. The Combustion Institute, Pittsburgh, pp 165–175

Bertin JJ, Ehrhardt ES, Gardiner WC Jr, Tanzawa, T (1975) Study of Improved Models for Laminar Shock Tube Boundary Layers in Chemically Reactive Test Gas. In: Modern Developments in Shock Tube Research, Proceedings of the Tenth International Shock Tube Symposium. Shock Tube Research Society, Japan, pp 595–604

Bowman CT, Hanson RK (1979) Shock Tube Measurements of Rate Coefficients of Elementary Gas Reactions. J. Phys. Chem. 83: 757

Brabbs TA, Zlatarich SA, Belles FE (1960) Limitations of the Reflected-Shock Technique for Studying Fast Chemical Reactions. J. Chem. Phys. 33: 307

Brabbs TA, Belles FE (1972) Experimental Study of Effects of Laminar Boundary Layers on Chemical-Kinetic Measurements in a Shock Tube. In: Shock Tube Research, Proceedings of the Eighth International Shock Tube Symposium. Chapman and Hall, London, p 24

Chang AY, Rea EC Jr, Hanson RK (1987) Temperature Measurements in Shock Tubes Using a Laser-Based Absorption Technique. App. Optics 26: 885

Ciezki H, Adomeit G (1990) Shock-Tube Investigation of the Ignition Delay on n-Heptane/Air-Mixtures in a High Pressure Shock Tube under Conditions Relevant to Diesel-Engine Combustion. In: Kim YW (ed) Current Topics in Shock Waves, 17th International Symposium on Shock Waves and Shock Tubes. American Institute of Physics, New York, pp 707–712

Davidson DF, Chang AY, DiRosa MD, Hanson RK (1993) A CW Laser Absorption Diagnostic for Methyl Radicals. J. Quan. Spec. Rad. Tran. 49: 559

Davidson DF, Hanson RK (1996) Real Gas Corrections in Shock Tube Studies at High Pressures. Israel J. Chem. 36: 321.

Davidson DF, Roehrig M, Petersen EL, DiRosa MD, Hanson RK (1996) Measurements of the OH A-X (0,0) 306 nm Absorption Bandhead at 60 atm and 1735 K. J. Quan. Spec. Rad. Tran. 55: 755

Davidson DF, Bates R, Petersen EL, Hanson RK (1998) Shock Tube Measurements of the Equation of State of Argon. Int. J. Thermophys. 19: 1585.

Fishburne E S, Bergbauer DM, Edse R (1964) Chemical Kinetics and the Reflected Shock Wave. Phys. Fluids 7: 1391

Flower WL (1976) Experimental Study of Nitric Oxide-Hydrogen Reaction Kinetics. Ph.D. Thesis, Department of Mechanical Engineering, Stanford University

Frenklach M, Wang H, Goldenberg M, Smith G P, Golden DM, Bowman CT, Hanson RK, Gardiner WC, Lissianski V (1995) GRI-Mech – An optimized Detailed Reaction Mechanism for Methane Combustion. GRI Topical Report No. GRI-95/0058

Fujii N, Koshi M, Ando H, Asaba *T* (1979) Evaluation of Boundary-Layer Effects in Shock-Tube Studies of Chemical Kinetics. Int. J. Chem. Kin. 11: 285

Gaydon AG, Hurle IR (1963) The Shock Tube in High-Temperature Chemical Physics. Reinhold, New York

Guinee MJ, Hewitt FA, Fussey DF, Milton BE, Palmer TF (1980) The Formation of Oxides of Nitrogen from $CH_4/O_2/N_2$ Mixtures. In: Shock Tubes and Waves, Proceedings of the 12th International Symposium on Shock Tubes and Waves. The Magnes Press, Jerusalem, pp 495–502

Hanson RK, Baganoff D (1970) Reflection of a Shock Wave into a Density Gradient. AIAA J. 8: 805

Hanson RK (1971) Shock Wave Reflexion in a Relaxing Gas. J. Fluid Mech. 45: 721

Hayashi AK, Goto M (1990) Low Temerature Ignition of N-Butane in a Tailored Condition behind a Reflected Shock Wave. In: Kim YW (ed) Current Topics in Shock Waves, 17th International Symposium on Shock Waves and Shock Tubes. American Institute of Physics, New York, pp 713–718

Ikui T, Matsuo K (1969) Investigations of the Aerodynamic Characteristics of the Shock Tubes (Part 1, The Effects of the Tube Diameter on the Tube Performance). Bull. JSME 12: 774

Ikui T, Matsuo K, Nagai M (1969) Investigations of the Aerodynamic Characteristics of the Shock Tubes (Part 2, On the Formation of Shock Waves). Bull. JSME 12: 783

Johnson CD, Britton D (1963) Shock Waves in Chemical Kinetics: The Use of Reflected Shock Waves. J. Chem. Phys. 38: 1455

Just Th, Schmalz F (1968) Measurements of Ignition Delays of Hydrogen-Air Mixtures under Simulated Conditions of Supersonic Combustion Chambers. AGARD Conference Proceedings No. 34, p 19

Kee RJ, Rupley FM, Miller JA (1989) Chemkin-II: A Fortran Chemical Kinetics Package for the Analysis of Gas-Phase Chemical Kinetics. Sandia National Laboratories Report, SAND89-8009

Koshi M, Asaba *T* (1979) Shock-Tube Study of Thermal Decomposition of Nitric Oxide between 2700 and 3500 K. Int. J. Chem. Kin. 11: 305

Lapworth KC, Allnutt LA, Pendlebury JR (1971) Temperature Measurements in Shock-Heated Carbon Monoxide by an Infrared Technique. J. Phys. D: App. Phys. 4: 759

Michael JV, Sutherland JW (1986) The Thermodynamic State of the Hot Test Gas behind Reflected Shock Waves: Implication to Chemical Kinetics. Int. J. Chem. Kin. 18: 409

Michael JV, Fisher JR (1990) Corrections for Non-Ideal Effects in Reflected Shock Waves at Low Mach Numbers. In: Kim YW (ed) Current Topics in Shock Waves, 17th International Symposium on Shock Waves & Shock Tubes. American Institute of Physics, New York, pp 210–215

Mirels H (1963) Test Time in Low-Pressure Shock Tubes. Phys. Fluids 6: 1201

Mirels H (1964) Shock Tube Test Time Limitation Due to Turbulent-Wall Boundary Layer. AIAA J. 2: 84

Napier DH, Nettleton M, Simonson JR, Thackeray DPC (1964) Temperature Measurement in a Chemical Shock Tube by Sodium-Line Reversal and C_2 Reversal Methods. AIAA J. 2: 1136

Outa E, Tajima K, Hayakawa K (1975) Shock Tube Flow Influenced by Diaphragm Opening (Two-Dimensional Flow Near the Diaphragm). In: Modern Developments in Shock Tube Research, Proceedings of the Tenth International Shock Tube Symposium. pp 312–319

Parkinson WH, Nicholls RW (1960) Spectroscopic Temperature Measurements in a Shock Tube Using CN as a Thermometric Molecule. Can. J. Phys. 38: 715

Petersen EL (1998) A Shock Tube and Diagnostics for Chemistry Measurements at Elevated Pressures with Application to Methane Ignition. Ph.D. Thesis, Department of Mechanical Engineering, Stanford University

Presley LL, Hanson RK (1969) Numerical Solutions of Reflected Shock-Wave Flowfields with Nonequilibrium Chemical Reactions. AIAA J. 7: 2267

Rea EC Jr, Salimian S, Hanson RK (1984) Rapid-Tuning Frequency-Doubled Ring Dye Laser for High Resolution Absorption Spectroscopy in Shock-Heated Gases. App. Optics 23: 1691

Rea EC Jr (1991) Rapid-Tuning Laser Wavelength Modulation Spectroscopy with Applications in Combustion Diagnostics and OH Line Shape Studies. Ph.D. Thesis, Department of Mechanical Engineering, Stanford University

Röhrig M, Petersen EL, Davidson DF, Hanson RK (1997) A Shock Tube Study of the Pyrolysis of NO_2. Int. J. Chem. Kin. 29: 483

Rothkopf EM, Low W (1974) Diaphragm Opening Process in Shock Tubes. Phys. Fluids 17: 1169

Rothkopf EM, Low W (1976) Shock Formation Distance in a Pressure Driven Shock Tube. Phys. Fluids 19: 1885

Rudinger G (1961) Effect of Boundary-Layer Growth in a Shock Tube on Shock Reflection from a Closed End. Phys. Fluids 4: 1463

Rudinger G (1969) Nonsteady Duct Flow: Wave-Diagram Analysis. Dover, New York

Simpson CJSM, Chandler TRD, Bridgman KB (1967) Effect on Shock Trajectory of the Opening Time of Diaphragms in a Shock Tube. Phys. Fluids 10: 1894

Skinner GB (1959) Limitations of the Reflected Shock Technique for Studying Fast Chemical Reactions. J. Chem. Phys. 31: 268

Strehlow RA, Cohen A (1958) Comment on Reflected Shock Wave Studies. J. Chem. Phys. 28: 983

Strehlow RA, Case CT (1961) Limitations of the Reflected Shock Technique for Studying Fast Chemical Reactions. J. Chem. Phys. 35: 1506

Tajima K, Outa E, Nakada G (1968) Some Investigations of Shock Tube Flow. Bull. JSME 11: 116

Tsuchiya S, Kuratani K (1965) Temperature Measurement of Argon Gas behind Reflected Shock Wave. J. Chem. Phys. 42: 2986

Vincenti WG, Kruger CH Jr (1965) Introduction to Physical Gas Dynamics. Krieger, Malabar

Warshay M (1968) Effects of Boundary Layer Buildup in Shock Tubes upon Chemical Rate Measurements. NASA TN D-4795

White DR (1958) Influence of Diaphragm Opening Time on Shock-Tube Flows. J. Fluid Mech. 4: 585